RSC Advances

PAPER

View Article Online
View Journal | View Issue

Cite this: *RSC Adv.*, 2017, **7**, 35982

Graphene oxide–metal nanocomposites for cancer biomarker detection†

Md. Azahar Ali, ‡[abc] Chandan Singh,‡[a] Saurabh Srivastava,[ae] Prasad Admane,[d] Ved V. Agrawal,[a] Gajjala Sumana,[a] Renu John,[c] Amulya Panda,[d] Liang Dong[b] and Bansi D. Malhotra *[e]

We report a universal protocol for the *in situ* bioinspired green synthesis of metal (Pd, Pt, Ag and Au) nanoparticles (mNPs) on simultaneously reduced graphene oxide (rGO) sheets using a black pepper extract (BPE) for quantification and kinetic analysis of epidermal growth factor receptor (ErbB2) for application to breast cancer diagnostics. The phytochemicals present in BPE were found to assist the reduction, stabilization, and surface addition of mNPs onto rGO sheets. The antioxidants present in the BPE assist the formation of a "green corona" on the surface of derived G-mNPs@rGO (G-Pd@rGO, G-Pt@rGO, G-Ag@rGO, and G-Au@rGO) sheets as corroborated by DLS and FT-IR experiments. These bioinspired derivatives provided biocompatible surfaces, resulting in higher cell viability compared to that of chemically derived composites, C-mNPs@rGO (C-Pd@rGO, C-Pt@rGO, C-Ag@rGO, and C-Au@rGO). Toxicity was found to be drastically reduced for green-corona assisted derivatives of GO due to strong antioxidant properties of the phytochemicals present in BPE. In addition, a comparative analytical study of the quantification and kinetics of breast cancer biomarkers using both G-mNPs@rGO and C-mNPs@rGO nanocomposites was carried out. The G-mNPs@rGO nanosheets can be employed for ultrasensitive detection of ErbB2 concentration from 1.0 fM to 0.5 μM.

Received 15th May 2017
Accepted 5th July 2017

DOI: 10.1039/c7ra05491b

rsc.li/rsc-advances

1. Introduction

With recent advances in graphene-based technology, graphene oxide (GO), a quasi-two-dimensional single layer of graphite[1,2] has been predicted to revolutionize point-of-care (POC) biosensors, intracellular analysis, bio-distribution, bio-imaging, and gene mapping.[3–7] According to the Lerf–Klinowski model, the reactive oxygen groups (carboxylic acid, epoxy, and hydroxyl) in GO sheets can be functionalized to facilitate binding of antibodies, DNA, sRNA,[8] *etc.* For fabrication of the nano-bioelectronic devices, the disrupted sp^2 bonding GO network can be restored *via* reduction reactions that may result in improved electrical conduction and transport characteristics utilizing the tunable chemistry and atomic structure of GO.[9–13] Many processes have been proposed for efficient restoration of the graphitic structures in GO.[11] In particular, reduction of GO produces higher electrical conductivity, that may lead to improved characteristics of a nano-bioelectronic device.

Chemical reductants (hydrazine, sodium borohydride, *etc.*) can be used to introduce heteroatomic impurities on the surface of GO sheets, and the formation of hydrazones, amines, aziridines, *etc.*, can affect the electronic structure of resulting reduced graphene oxide (rGO).[12,13] The structural damage to the GO sheets arising from the release of carbon dioxide during the process of thermal reduction may decrease the ballistic transport path length by introducing scattering sites.[14] The toxicity of chemically derived rGO is known to be harmful for biological systems[15,16] and is a major concern for both *in vitro* and *in vivo* applications that require direct contact with human cells.[17] The trace amounts of these toxic reductants on rGO surfaces may lead to a loss of protein structure and activity.[18] In addition, the rGO synthesized using chemicals like $NaBH_4$ have been found to be very toxic leading to depletion of the mitochondrial membrane potential and promote the production of intra cellular reactive oxygen species (ROS).[19–21]

Bioinspired green reduction of GO and metal nanoparticles (mNPs) using plant extracts (phytochemicals) is a promising approach to obtain biocompatible nanomaterials.[22]

[a]*Department of Science & Technology Centre on Biomolecular Electronics, Biomedical Instrumentation Section, CSIR-National Physical Laboratory, New Delhi 110012, India*
[b]*Department of Electrical and Computer Engineering, Iowa State University, Ames, IA, 50011, USA*
[c]*Department of Biomedical Engineering, Indian Institute of Technology Hyderabad, Kandi, Sangareddy, Telangana 502285, India*
[d]*National Institute of Immunology, Aruna Asaf Ali Marg, New Delhi 110067, India*
[e]*Department of Biotechnology, Delhi Technological University, Main Bawana Road, Delhi 110042, India. E-mail: bansi.malhotra@gmail.com; Fax: +91-11-45609310; Tel: +91-11-45609152*

† Electronic supplementary information (ESI) available. See DOI: 10.1039/c7ra05491b

‡ These authors have contributed equally.

Functionalization with phytochemicals may diminish toxicity by providing a biocompatible layer due to the presence of different biomolecules leading to biocompatible rGO.[21] Thus, biologically derived rGO and nanocomposites offer a sustainable solution for reduced toxicity.[20] The phytochemical rich species with immense reducing capability may function as universal reducing agents for GO and noble metal salts. In addition, the bioinspired green reduction method offers the advantage of a one-step synthesis of nanomaterials in comparison to the conventional multi step synthesis process of utilizing different chemicals as reducing and stabilizing agents.[23] Green reduction with biological species is a mild process that may prevent agglomeration of rGO and composites.[24–26] Interaction of a biological molecule with a nanostructured material may facilitate the formation of corona that may significantly influence the mode of interaction with target biomolecules and modulate cytotoxicity of the nanomaterial.[27] The phytochemical-derived, green-corona-mediated interfaces may also promote immobilization of biomolecules (*e.g.* antibodies) by establishing a biocompatible layer that may prevent conformational changes of the binding sites and hence maintain structural integrity of a protein/antibody. Due to presence of the different functional groups, phytochemicals may offer increased binding sites for the desired antibodies resulting in a high performance biosensing device.

The natural spice black pepper (*Piper nigrum*) is a seasoning component that can be exploited as a reducing, surface-modifying, and stabilizing agent for uniform decoration of mNPs to the simultaneously reduced GO. In a phytochemical reduction, polyphenols, on oxidation, are converted to quinones.[26,27] We present a bioinspired green approach for simultaneous *in situ* reduction of the noble metal (Pd, Pt, Ag, and Au) nanoparticles and GO using black pepper (BP) extract. As shown in the Fig. 1 and Scheme S1,† BP contains a large number of phytochemicals including piperine, hinkonin, pipertine, piperolin, piperide *etc.* These phytochemicals rich BP may work as efficient reducing agents for the green synthesis of metal nanoparticles as reported by Augustine *et al.*[28] Apart from working as reducing agent, it also helps in stabilizing nanoparticles suspension in aqueous medium over a longer period of time. In this regard, utilization of BP extract for the simultaneous reduction of GO and noble metal salts to achieve mNPs decorated rGO sheets, is an eco-friendly route to obtain a biocompatible nanocomposite for biosensing application. In addition to these phytochemicals present in the BP that are known to have antioxidant properties, naturally occurring antioxidants such as piperine are reported to be very effective in inhibiting the induction of carcinogenesis.[29,30] Piperine is known to be the main component responsible for the biocompatible behavior of BP, as it promotes inhibition of the reactive oxygen species, the main cause of toxicity of the carbon based materials in cell culture medium.[31,32]

The availability of oxygenated functional groups on the basal and edge plane of the GO make these areas for growth and nucleation of mNPs.[33–36] mNPs conjugated with ErbB2 antibodies may perhaps be utilized to obtain improved biosensor efficacy.[37] In this report, we present results of the investigations relating to the toxic effect of rGO: both chemically derived C-mNPs@rGO (C-Pd@rGO, C-Pt@rGO, C-Ag@rGO, and C-Au@rGO) and bioinspired green-derived G-mNPs@rGO (G-Pd@rGO, G-Pt@rGO, G-Ag@rGO, and G-Au@rGO) composites in the presence of MCF-7 cell line using the MTT assay. We have also performed a comparative analysis of bioinspired- and chemically derived mNPs@rGO nanosheets for protein binding and breast cancer biomarker (epidermal growth factor receptor 2; ErbB2) detection using antibody–antigen interactions.

2. Experimental

2.1 Chemicals

Graphite powder flakes (50 μm, >99.99 wt%) were obtained from Sigma Aldrich, USA. Various precursors of metals including $PdCl_2$ (S D Fine chemicals, Mumbai), $H_2PtCl_6 \cdot 6H_2O$ (Johnson Matthey UK), $AgNO_3$ and $HAuCl_4 3H_2O$ were purchased from Sigma Aldrich, USA. Epidermal growth factor receptor (ErbB2) human recombinant and rabbit polyclonal ErbB2 antibody (solubility in phosphate-buffered saline containing 30% glycerol, 1% BSA and 0.02% thimerosal) were obtained from Bio-Vision, USA. The black peeper was purchased from the local market in New Delhi, India. The breast cancer cells (MCF-7) were procured from National Centre for Cell Sciences (NCCS), Pune, India.

2.2 Preparation of black pepper extract

To prepare BPE, 10 g of black pepper seed was washed several times with deionized (DI) water to remove any impurities and then immersed in 40 mL of DI water for 12 h at room temperature (27 °C). The percentage distribution of phytochemical components present in BP extract (BPE) is shown in the pie diagram (Scheme S1, ESI†). This solution was filtered using filter paper (Whatman Grade no. 40) and then centrifuged at 8000 rpm for 15 minutes and supernatant was collected and stored at 4 °C until use.

2.3 Bioinspired synthesis of G-mNPs@rGO hybrids

Prior to green reduction, GO was synthesized according to a procedure reported in literature.[38] Graphite flakes (2.0 g) and $KMnO_4$ (12 g) were added to a mixture of concentrated H_2SO_4 and H_3PO_4, (9 : 1 v/v, 240 mL/26.7 mL). $KMnO_4$ was added slowly over 15 min to prevent any explosion due to exothermic nature of reaction. The reaction mixture was kept for about 12 h at 50 °C with magnetic stirring. The reaction was quenched by adding 300 mL of ice with 2.5 mL of H_2O_2 (30% w/w). A yellow colored slurry was obtained, centrifuged and filtered using HCl (30% w/v) and finally washed with distilled water until the pH ~7.0 was reached. To obtain a solid, dry powder of GO, the product was dried at 65 °C.

The green synthetic strategy aimed at achieving a single step simultaneous, natural product derived green reduction of GO and metal salts (Pd^{2+}, Pt^{4+}, Ag^{+}, and Au^{3+}) resulting in a G-rGO platform covered with corresponding nanoparticles using BPE for each metal was as follows: G-Pd@rGO composite preparation, 5 mg of $PdCl_2$ was added to 10 mL of GO aqueous

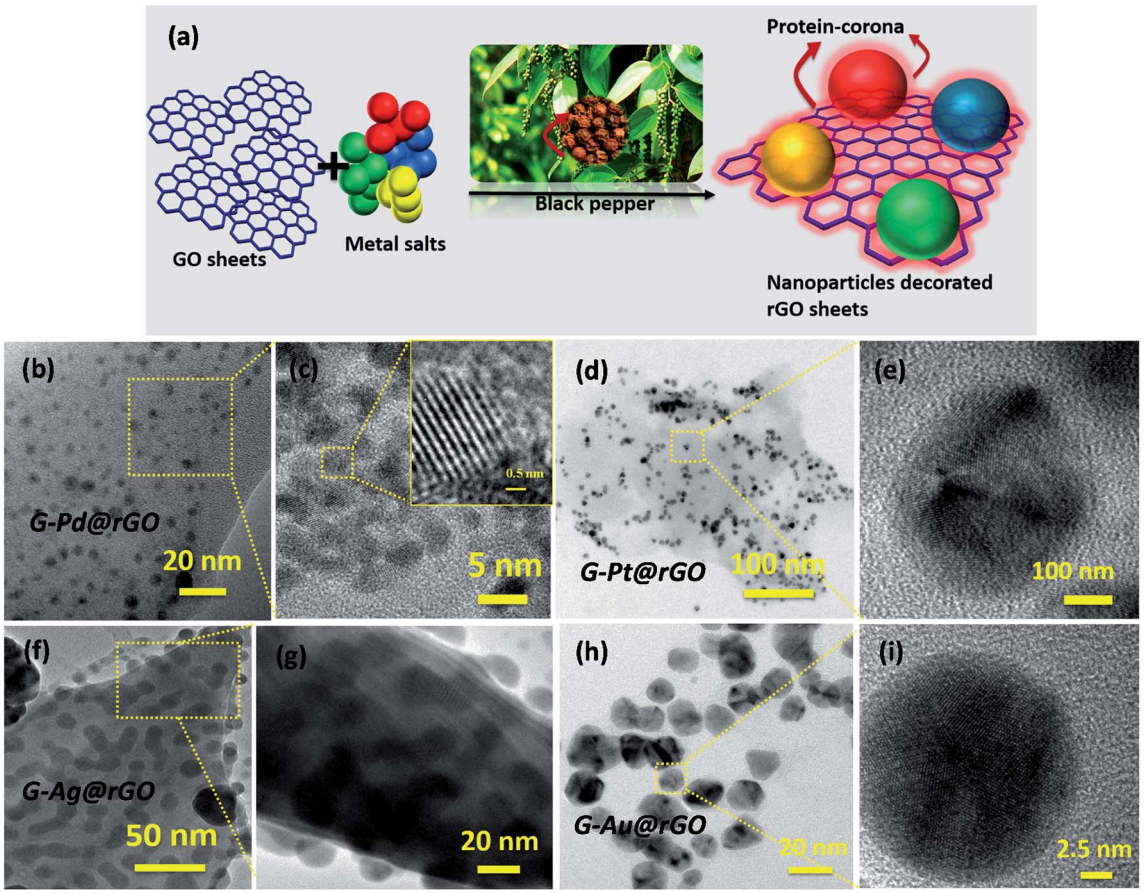

Fig. 1 (a) Formation of protein-corona on the surface of mNPs@rGO sheets. (b and c) G-Pd@rGO nanocomposite, inset of (c) shows a high-resolution image of G-Pd@rGO, (d) G-Pt@rGO nanocomposite, (e) magnified image of G-Pt@rGO nanocomposite. (f and g) G-Ag@rGO nanocomposite and (h and i) G-Au@rGO nanocomposite.

suspension (1.0 mg mL^{-1}) and the resulting mixture was aged for 30 min at 50 °C to allow the interaction of palladium ions with the dispersed GO surface. Subsequently, BPE (2.5 mL) was added drop wise to the prepared suspension that was kept at 80 °C for 12 h to reduce both the GO and Pd(II) complex.

Synthesis of G-Pt@rGO, 10 mL of an aqueous suspension of GO (1 mg mL^{-1}) was mixed with 10 mL of $H_2PtCl_6 \cdot 6H_2O$ (7 mM) followed by addition of 2.5 mL of BPE solution and was kept at 70 °C on a magnetic stirrer for 10 h. The light brown colour of this solution changed to black after 10 h resulting into simultaneous reduction of both Pt^{4+} ions and GO. In case of the G-Au@rGO, 1 mL of $AuCl^{4-}$ (10 mM) was mixed into 10 mL of GO aqueous solution (1.0 mg mL^{-1}), and subsequently, 2.5 mL of BPE solution was added drop wise, and the reaction temperature was maintained at 50 °C for 12 h. Similarly, the G-Ag@rGO composite was synthesized by adding 10 mL of $AgNO_3$ solution (5 mM) into 10 mL of an aqueous suspension of GO (1 mg mL^{-1}) plus 2.5 mL of BPE solution and the reaction was conducted for 8 h.

For conversion of GO to rGO, 2.5 mL of BPE solution was added to 10 mL of GO (1.0 mg mL^{-1}) solution and the reaction was maintained at 80 °C for 8 h. All the four resulting nanohybrids and BPE derived rGO were washed with distilled water and centrifuged (5000 rpm) to remove any residue from the solution. For natural synthesis of the different metals such as Pd, Pt, Ag, and Au on rGO nanosheets, we varied the reaction times and temperatures due to their different nucleation energies and growth mechanism.

2.4 Chemical synthesis of C-mNPs@rGO

We adopted the protocols available in literature for the chemical synthesis of AuNPs, AgNPs, PtNPs, and PdNPs on rGO.[39–42]

2.5 Fabrication of biosensing platforms

To prepare biosensing electrode, 20 μL of a colloidal suspension of G-mNPs@rGO was uniformly spread onto hydrolyzed indium tin oxide (ITO) coated glass substrate and kept at 60 °C for 4 h. The electrode was treated with EDC–NHS solution for about 4 h to activate the functional groups (–COOH) present on the rGO sheets. The EDC (0.2 M) acted as a coupling agent and the NHS (0.05 M) worked as an activator. The EDC–NHS coupling chemistry was used to bind rGO to antibody (anti-ErbB2) *via* covalent amide bond formation on transducer surface. Anti-ErbB2 solution (0.02 mg mL^{-1}) was spread on the G-mNPs@rGO surface overnight in a humidity chamber at 4 °C followed by washing with PBS to remove any unbound anti-ErbB2. The amide (CO–NH) groups were formed between the

–COOH groups of G-mNPs@rGO and $–NH_2$ terminal groups of anti-ErbB2. Lastly, 20 μL of BSA (2 mg dL^{-1}) was used to block the non-specific adsorption of anti-ErbB2 (Scheme 1).

2.6 Cytotoxicity tests

Human breast cancer cells MCF-7 were maintained in DMEM containing 10% FCS (Gibco, Invitrogen) and 1% antibiotic (Sigma A5955). Prior to seeding, the cells were dissociated with non-enzymatic cell dissociation buffer (Sigma C5789) and re-suspended in fresh media. 8000 cells per well were seeded in 96 well plates and left overnight for attachment. The colloidal suspensions of GO, G-rGO, G-Pd@rGO, G-Pt@rGO, G-Ag@rGO, G-Au@rGO, C-Pd@rGO, C-Pt@rGO, C-Ag@rGO, and C-Au@rGO were serially diluted by 3 fold in the serum free medium. The cells were treated with undiluted and diluted compounds for 24 h at 37 °C in a CO_2 incubator with untreated cells as control. The viability was assessed by MTT assay carried out by incubating cells with an MTT reagent (0.05 mg mL^{-1} in serum free medium) for 4 h at 37° in CO_2 incubator. The formazan crystals formed were dissolved in 100 μL DMSO. The plates were incubated for 15 minutes at room temperature (25 °C) and absorbance was measured at 570 nm with a reference of 630 nm. MCF-7 cells when treated with GO, G-Pd@rGO, G-Pt@rGO, G-Ag@rGO, G-Au@rGO were examined for viability and LD (lethal dose) 50 values were calculated on the basis of viability curves. Viability was determined as percentage of absorbance of treated samples *versus* untreated samples. GO, G-rGO, Pd@rGO, Pt@rGO, Ag@rGO and Au@rGO with and without green reduction showed dose dependent toxicity throughout the wide range of concentration (19 μg mL^{-1} to 500 μg mL^{-1}). The LD 50 values for nanocomposites G-Pt@rGO and G-Ag@rGO were determined to be 56 μg mL^{-1} and 80 μg mL^{-1}, respectively. The G-Pd@rGO nanocomposite exhibited the highest toxicity compared to other green nanocomposites and all the cells were affected even at concentrations as low as 18.5 μg mL^{-1}. The G-Ag@rGO nanocomposite showed the highest viability at concentrations of 56 and 167.67 μg mL^{-1}. The BPE showed no toxicity and cells were found to be viable even at high concentration of 500 μg mL^{-1} arising due to presence of available biological components. A histogram plot indicated the value of LD 50 for GO and all the composites and it varied as G-rGO > G-Ag@rGO > GO > G-Pt@rGO > G-Au@rGO > G-Pd@rGO (Fig. S1, ESI†). The incorporation of metal nanoparticles on G-rGO surface resulted in increased surface area which perhaps facilitated binding with cell surface. Further, cell viability of chemically derived reduced graphene oxide (C-rGO) and other composites C-mNPs@rGO (C-Pd@rGO, C-Pt@rGO, C-Ag@rGO and C-Au@rGO) were performed under similar experimental conditions as mentioned above. The cell viability of C-rGO found to be very low as the residues of $NaBH_4$ present on the surface of C-rGO, perhaps resulted in the depletion of mitochondrial membrane generating higher reactive oxygen species. The chemically derived composites showed cytotoxicity in the concentration manner as the C-Ag@rGO and C-Pd@rGO exhibited the lowest cell viability at the 167.6 μg mL^{-1}, while at the concentration of 55.56 μg mL^{-1} cell viability for C-Ag@rGO was found to be very less as compared to chemically derived composites.

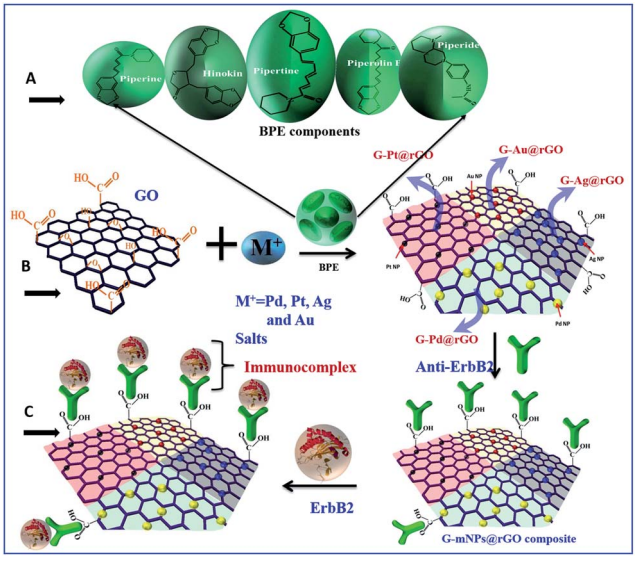

Scheme 1 Pictorial representation of G-mNPs@rGO platforms (A) chemical structure of various biomolecular components in BPE, (B) simultaneous green reduction of metal salts and GO using BPE and (C) immobilization of antibodies on G-mNPs@rGO platforms for breast cancer detection.

2.7 Instrumentation

The growth of metal nanoparticles (Pd, Pt, Ag and Au), GO, G-rGO and mNPs@rGO nanocomposites was monitored using UV-visible spectrometer and transmission electron microscopy (TEM; JEOL JEM-2000 EX). The green reduction of GO was confirmed by Raman spectroscopy (WiTec, Germany that had a laser light source of 532 nm wavelength) and Fourier transform infrared spectroscopy (FT-IR; Perkin-Elmer, Model 2000). The elementary (EDX) studies were investigated using scanning electron microscope (SEM, LEO-440). The electrochemical studies such as cyclic voltammetry, electrochemical impedance spectroscopy were performed using an Autolab Potentiostat/Galvanostat (Electrochemical analyzer; AUT-84275) in PBS at pH 7.4 containing 5 mM of $[Fe(CN)_6]^{3-/4-}$ as a redox species.

3. Results and discussion

3.1 Structural and morphological analysis

Transmission electron microscopy (TEM) studies were used to unravel the morphology, shape, and size of the green-reduced GO (G-rGO), metal NPs, and metal–rGO composites [Fig. 1]. The G-rGO images show wrinkles and folds, arising due to π–π interactions of the sheets [Fig. S2†]. In addition to this, oxygen moieties present on the GO surface perhaps provided nucleation sites for growth of the metal NPs. On the basis of the density functional theory (DFT), the most highly preferred locations for the metals on graphene could be predicted[43] as the center of the hexagonal ring position (H sites), corner sites directly above C atoms (T sites), and the bridge sites above C–C

bonds (B sites) [Fig. S3†]. The oxygen groups provided a negatively charged GO surface that perhaps interacted with the free Pd^{2+}, Pt^{4+}, Ag^{+}, and Au^{3+} ions *via* electrostatic interactions.[43–45]

The formation of a green-corona on G-mNPs@rGO nanosheets is demonstrated in Fig. 1(a). The images [Fig. 1(b and c)] show results of the HRTEM investigations of G-Pt@rGO composites. After reduction, the PdNPs with an average size of ~7 nm appear to be partially uniformly distributed on GO sheets (b and c). Similarly, rGO sheets perhaps provided the nucleation site for uniform growth and distribution of PtNPs [Fig. 1(d and e)]. The image (c) shows the 3D "top-like" structure (size: ~15 nm; G-Pt@rGO) of PtNPs. The AgNPs (size: ~10 nm) were uniformly distributed and attached to the G-rGO sheets after green reduction (Fig. 1(f and g)). Fig. 1(h and i) shows different 3D structures including triangular, spherical, and hexagonal shapes of AuNPs (image i) after green reduction of the Au salt. More details have been described in ESI.†

The TEM studies on the chemically derived mNPs and rGO composites including C-Pd@rGO, C-Pt@rGO, C-Ag@rGO, and C-Au@rGO [Fig. S4†] were carried out. In all cases, the multistep synthesis process utilizing different chemicals as reducing and stabilizing agents resulted in non-homogeneous distribution and non-selective growth of mNPs on the surface of GO sheets. The bioinspired green synthesis is thus, a potential approach for uniform coverage and growth of mNPs on rGO sheets.

The results of elemental analysis studies revealed that G-mNPs@rGO sheets interactions could be quantified [see Fig. S5† with explanation]. The histogram plot depicts (Fig. S5†) the atomic ratio and weight percentage of the various nanocomposites. We also conducted the TEM studies on the chemically derived mNPs and rGO composites including C-Pd@rGO, C-Pt@rGO, C-Ag@rGO, and C-Au@rGO [Fig. S5 (ESI†)].

3.2 Spectroscopic analysis

To confirm the formation of green derived noble metal, rGO, and G-mNPs@rGO, Fourier transform infra-red (FT-IR), UV-visible and Raman studies were conducted [Fig. 2]. The results of FT-IR studies revealed the presence of functional groups in chemically exfoliated graphite, natural product derived rGO nanosheets and BPE [Fig. 2(a and b)]. An intense peak seen at 1600 cm^{-1} was assigned to the O=C–N (amide bond) and was perhaps due to the presence of piperine, piperolein B, piperaide, and piperettine in BPE leading to the formation of green-corona on the surface of the natural product derived nanomaterials. In the FT-IR spectra of G-rGO, an additional peak appeared at 1586.2 cm^{-1} due to the O=C–N stretch resulting from BPE coating of the GO surface. The peak found at 1235 cm^{-1} indicated C–N stretching in the natural product derived G-rGO. To further confirm, Raman spectroscopy was utilized to corroborate the green reduction of GO [Fig. 2(c)]. The increased I_D/I_G intensity ratio of GO suggested decrease in the average size of the sp^2 domains on reduction of exfoliated GO that created numerous graphitic domains that were perhaps smaller than in the exfoliated GO. Table S1† shows the peak positions of the G-band as well as their left and right widths at half-maximum. The crystallite size of G-rGO was smaller (22.3 nm) compared to that of GO (22.9 nm) due to reduction of oxygen functionalities during green reduction. More details on the results of FT-IR and Raman studies are given in the ESI.†

To investigate the nucleation and growth of metal NPs, we performed the UV-visible spectroscopic measurements at various steps during green synthesis of G-mNPs@rGO composites. The results of the UV-visible studies [Fig. 3(d) and S6†] were further confirmed *via* simultaneous *in situ* reduction of metal salts (Pd, Pt, Ag, and Au) on GO sheets. The characteristic peaks of G-rGO and GO found at 270 nm and 230 nm (due to π–π transitions), respectively, suggested the reduction of GO sheets. The observed shift in wave number for G-rGO could be assigned to the reduction of functional groups by the green method. The green reduction of GO–Au salt resulted in two peaks at 270 nm and 539 nm arising due to the formation of G-rGO and AuNPs, respectively. The peak at 539 nm was due to inherent plasmonic properties of the AuNPs. More details on the results of UV-visible studies are demonstrated in Fig. S6.† Dynamic light scattering (DLS) measurements were performed to measure the size of the synthesized GO and its green derivatives (see Fig. S7† for explanation). The value of zeta potential of the G-Pd@rGO, G-Pt@rGO, G-Ag@rGO, and G-Au@rGO was found to be as −14.7, −16.4, −19.0, and −2.31 mV, respectively (Table S2†).

3.3 Cell viability studies

Effects on cell viability of the different derivatives of GO obtained *via* green and chemical routes were assessed using MCF-7 cell lines. Natural product modified GO and mNP composites, G-rGO, G-Pd@rGO, G-Pt@rGO, G-Ag@rGO, and G-Au@rGO were found to be less toxic than their chemically derived counterparts. The un-reduced GO was used as a control during all the experiments. The nanocomposites such as G-Pt@rGO and G-Ag@rGO were found to have mild toxicity and their LD (lethal dose) 50 values were less than 100 μg mL^{-1}. The observed high toxicity of $NaBH_4$ in C-rGO (chemically derived GO) was in agreement with the report available in literature[16] and was perhaps due to depletion of the mitochondrial membrane potential, resulting in enhanced production of intracellular reactive oxygen species (ROS). In comparison, the BP derived G-rGO was found to be non-toxic and cell viability was determined to be very high at 500 μg mL^{-1} (Fig. 3). This was attributed to the formation of a "green corona" on the surface of G-rGO prevents oxidative stress.[19–21]

Biomolecules such as proteins and enzymes are known to mitigate the toxicity by decreasing ROS. It appeared that green phytochemical residues attached onto the surface of the G-rGO perhaps played an important critical role in the observed higher cell viability.[16,46] The non-toxic behavior of BPE was confirmed because cell viability was maintained at even higher concentrations. As mentioned earlier, piperine is a major chemical component of BPE and is known to have strong antioxidant properties.[24] Antioxidants such as piperine are known to protect against oxidative damage by inhibiting generation of ROS and free radicals.[29–31,47] The green corona incorporating these antioxidants thus played an important role in decreasing the

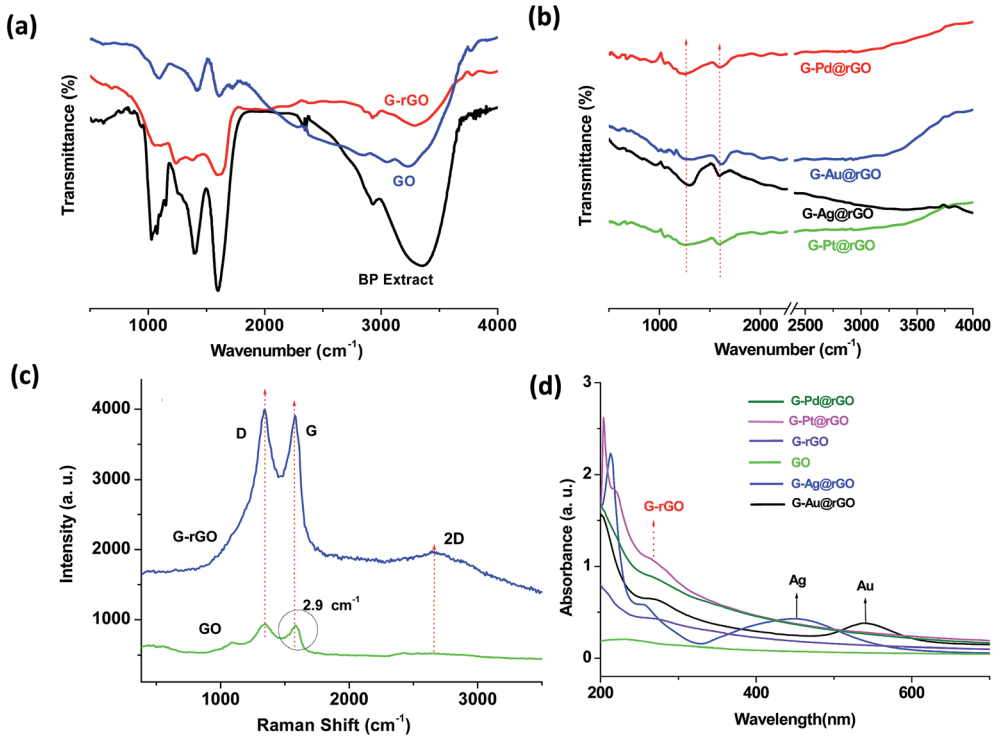

Fig. 2 FT-IR spectra of GO, G-rGO, BPE, G-mNPs@rGO nanocomposites (a and b). Raman spectra of GO before (green curve) and after (blue curve) green reduction (c), and UV-visible spectra of GO, G-rGO, BPE, G-mNPs@rGO nanocomposites (d).

cytotoxicity. The results of microscopic imaging studies suggested that green derived G-mNPs@rGO interacted with the cell surface [Fig. 3(a)]. The results of cell viability (%) obtained for the various green and chemically reduced nanomaterials are shown in Fig. 3(b). The histogram plot shows that the maximum value of lethal dose 50 (LD_{50}) was observed for G-Au@rGO NPs [Fig. S1 (ESI†)]. All the chemically prepared compounds, C-mNPs@rGO, showed high toxicity across the concentration range (19 μg mL^{-1} to 500 μg mL^{-1}) compared to that of G-mNPs@rGO. Cell viability follows the order G-rGO > G-Au@rGO > G-Ag@rGO > G-Pd@rGO > G-Pt@rGO. These metal–rGO composites were not washed off even after rinsing with PBS, indicating strong interaction with the cell membrane resulting due to presence of electrostatic interaction between negatively charged cell surfaces and positively charged G-mNPs@rGO particles as shown by the results of zeta potential experiments.

3.4 Electrochemical studies

The results of cyclic voltammetry (CV) studies conducted on GO revealed that the oxidation peak current (435 μA) at 0.4 V, increased to 462 μA [Fig. 4(a)] for G-rGO due to reduction of the functional groups. The negatively charged species (hydroxyl, carboxyl, epoxy *etc.*) perhaps repelled the similarly charged ferro/ferricyanide ions during oxidation/reduction resulting in decreased current. The observed higher current in G-rGO was perhaps due to the presence of phytochemicals on its surface that may facilitate heterogeneous electron transfer (HET) between the electrode and electrolyte. The effective electrochemical area (EAeff) was estimated using the Randles–Sevcik equation *i.e.* $i_p = 2.6 \times n^{3/2} A_{eff} D^{1/2} C \nu^{1/2}$; where i_p, n, ν, A_{eff}, D and C are the peak current, the number of electrons appearing in half-reaction for the redox couple ($n = 1$), the scan rate, the effective electrochemical area, the diffusion coefficient, and the surface concentration, respectively. The effective electrochemical area (EA_{eff}) of G-rGO (0.544 cm^2) was higher than that of GO (0.498 cm^2). In GO electrode, the diffusion co-efficient of $[Fe(CN)_6]^{3-/4-}$ decreased to 3.35×10^{-5} cm^2 s^{-1} compared to G-rGO electrode (3.88×10^{-5} cm^2 s^{-1}) due to the large number of negative charges at GO.

The incorporation of AgNPs into the G-rGO sheets resulted in increased oxidation peak current (689 μA). The AgNPs perhaps influenced the oxidation/reduction of $[Fe(CN)_6]^{3-/4-}$ due to excellent electrocatalytic activity of redox species suggesting higher electron transfer kinetics. The values of diffusion co-efficient (8.52×10^{-5} cm^2 s^{-1}) and EA_{eff} (0.846 cm^2) were found to be increased due to addition of AgNPs to the G-rGO surface. Table S3† describes results of the electrochemical studies conducted using the various electrodes. In the presence of metal nanoparticles at the G-rGO surface, the oxidation peak current, diffusion co-efficient and EA_{eff} were found to be enhanced as compared to those of the GO and G-rGO based electrodes. The higher EA_{eff} of mNPs–G-rGO was due to incorporation nano-sized metal nanoparticles into G-rGO sheets which may facilitate higher electron transfer properties as compared to the bare G-rGO. The oxidation current, diffusion co-efficient and EA_{eff} of G-Ag@rGO composite were the highest

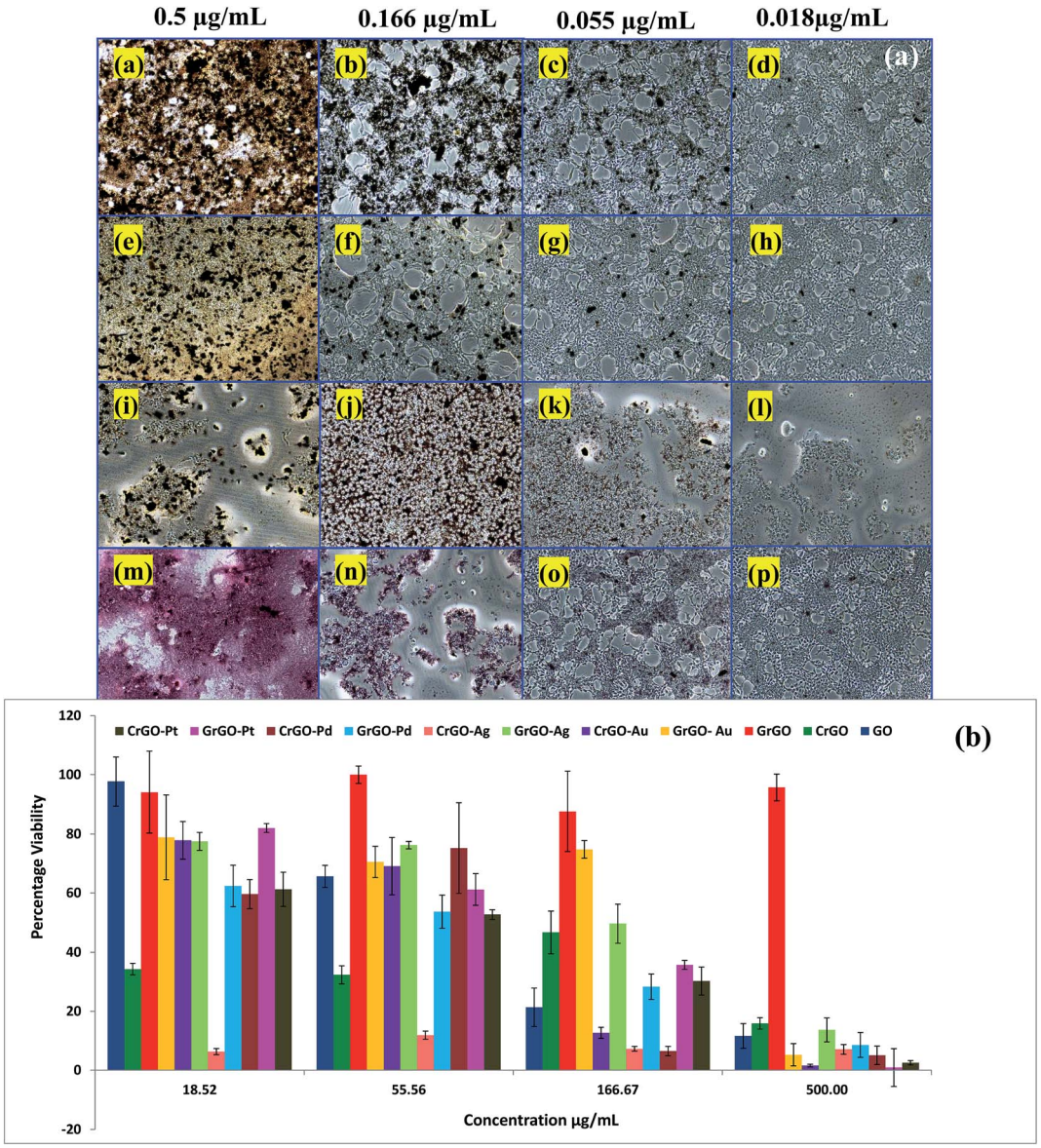

Fig. 3 (a) Optical images of MCF-7 cells treated with G-Pd@rGO (a–d), G-Pt@rGO (e–h), G-Ag@rGO (i–l) and G-Au@rGO (m–p) at different concentrations. (b) Histogram plot of cell viability (%) for various green and chemically derived composites.

for all these composites. Thus, AgNPs on the G-rGO surface facilitated electron transfer most effectively.

The value of HET rate constant (K_e) obtained for GO was higher than that of the G-rGO electrode due to reduction of the oxygen functional groups [Fig. 4(b)]. It appeared that the incorporation of the mNPs influenced the charge transfer properties of the nanocomposites resulting in variation of HET during redox reaction of $[Fe(CN)_6]^{3-/4-}$. The value of HET obtained for these composites followed the order: G-Ag@rGO > G-Au@rGO > G-Pt@rGO > G-Pd@rGO composite. The higher HET value of G-Ag@rGO electrode was perhaps due to intrinsic catalytic properties of AgNPs onto G-rGO nanosheets and its higher density of AgNPs on G-rGO sheets as compared to other metal nanoparticles onto G-rGO nanosheets as evidenced by TEM studies (Fig. 1).

The value of charge transfer resistance (R_{ct}), determined using electrochemical impedance spectroscopy (EIS), was found to be 1.45 kΩ for GO, which was higher than that for G-rGO (1.03 kΩ) [Fig. S8†]. The presence of increased number of functional groups (carboxyl, hydroxyl, epoxy *etc.*) in GO resulted in higher R_{ct}. It appears that negatively charged GO sheets on the surface of electrode perhaps repelled the negatively charged ferri/ferrocyanide ions in bulk solution.

3.5 Detection of breast cancer biomarkers

In order to estimate the concentration of breast cancer biomarker antigen, EIS measurements were performed as a function of ErbB2 concentration (1.0 fM to 0.5 µM) using both bioinspired green and chemically derived metal–rGO immunoelectrodes. Fig. S9(a–d) and S10(a–d)† show the spectra

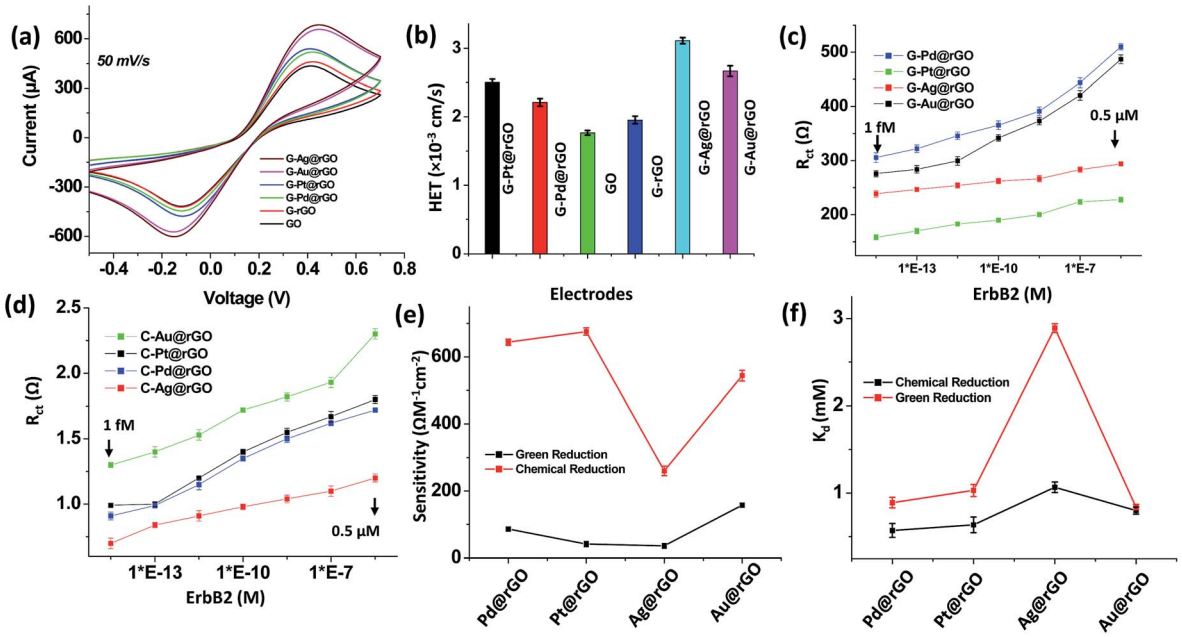

Fig. 4 (a) Cyclic voltammetry (CV) studies of various electrodes prepared on ITO coated glass substrates in phosphate buffer saline at pH 7.4 (50 mM, 0.9% NaCl) containing $[Fe(CN)_6]^{3-/4-}$ (5 mM) and (b) HET values with different electrodes. Plots of R_{ct} (charge transfer resistance) values and ErbB2 concentration (1.0 fM to 0.5 μM) for Pd@rGO/ITO, Pt@rGO/ITO, Ag@rGO/ITO, and Au@rGO/ITO electrodes with immobilized anti-ErbB2 (c) after green reduction and (d) after chemical reduction. (e) Sensitivity plots for various composite based immunoelectrodes using green or chemical reduction. (f) Dissociation constant (K_d) plots obtained from Hill plots for green and chemical reduction.

obtained for bioinspired and chemically derived immunoelectrodes as a function of ErbB2 concentration (ESI†). The semicircle (charge transfer resistance) of the Nyquist plot increased with increasing ErbB2 concentration. The immunocomplex formed between antigen and antibody on the transducer surface perhaps blocked the charge transfer due to redox reaction of the $[Fe(CN)_6]^{3-/4-}$ ions resulting in higher R_{ct}. The variation of R_{ct} values obtained for each of the electrode as a function of ErbB2 is shown in Fig. 4(c and d). The observed variation in biosensing parameters for the mNPs on G-rGO nanosheets can be attributed to the intrinsic electron transfer properties of the nanocomposite (Fig. 4(c)). These biosensors can detect a minimum 1.0 fM concentration of cancer biomarker, and below this concentration sensors do not show a significant change with zero concentration of biomarker. These nanocomposite-based electrodes can be used to detect low concentration (1 fM) of cancer biomarker (ErbB2) in the wide concentration range of 1 fM to 0.5 μM.

Fig. 4(e) shows the variation of sensitivity determined for both bioinspired and chemically derived composites. For green derived G-mNPs@rGO composites, the high sensitivity was observed in case of the G-Au@rGO and G-Pd@rGO as compared to that of G-Ag@rGO and G-Pt@rGO. The sensitivity of the G-mNPs@rGO composites for ErbB2 detection followed the order: G-Au@rGO > G-Pd@rGO > G-Pt@rGO > G-Ag@rGO. These results suggested that strong amide bonds between G-rGO and anti-ErbB2, and interaction of the antibody with mNPs played an important role in the performance of these nanocomposites based biosensors. The chemically synthesized C-mNPs@rGO composites showed higher impedance signal as compared to that of G-mNPs@rGO due to non-uniform distribution of mNPs on C-rGO sheets causing hindrance to bulk electron diffusion from the electrolyte solution. The sensitivity of the chemically derived C-mNPs@rGO composites for ErbB2 detection followed the order: C-Pt@rGO > G-Pd@rGO > G-Au@rGO > G-Ag@rGO.

The zeta potential value measured for G-Au@rGO (−2.31 mV) indicated decreased electrostatic attraction with anti-ErbB2, since anti-ErbB2 perhaps contributed to the negative charge of the biomolecule [Table S2†].[48] This perhaps facilitated enhanced loading of the ErbB2 antibodies on the surface of AuNPs compared to other nanoparticles. The lower zeta potential of the G-Au@rGO, as compared to other nanocomposites offered improved electrostatic interaction with the anti-ErbB2 and its coverage on the G-Au@rGO. In addition, G-Au@rGO showed maximum cell viability as evidenced by cell proliferation studies offering the most favorable surface for anti-ErbB2 attachment compared to other nanocomposites resulting in increased sensitivity and stability of the device. The G-Ag@rGO showed a maximum surface charge of −19.0 mV that perhaps resulted in increased repulsion with anti-ErbB2 molecules and the enhanced toxicity of G-Ag@rGO composite caused loss of protein structure that perhaps led to low sensitivity as compared to that of other composites [Table S4†]. The attachment of mNPs onto G-rGO resulted in improved electrochemical properties leading to better biosensor efficacy for cancer diagnostics compared to those reported in literature [Table S4†].[49–51] The lower impedance response of the BPE derived composites compared to those of derived chemically was due to uniform coverage of ultrafine mNPs on G-rGO

nanosheets, which enhanced electrochemical charge transfer. In addition, some of the residues of phytochemicals used in green reduction mentioned in Scheme S1 (ESI†) exhibited enhanced charge transfer properties leading to a decreased impedance signal. The bioinspired derived G-mNPs@rGO composites can thus be used to detect very low concentrations of cancer biomarker (1.0 fM) due to favorable conjugation with antibodies.

The binding kinetics of antibody–antigen interactions was analyzed using Hill plots as [Fig. 4(f) and ESI†].[52] The value of dissociation constant (K_d) followed the order: G-Ag@rGO > G-Au@rGO > G-Pt@rGO > G-Pd@rGO for bioinspired and chemically derived composites. The higher K_d of AgNPs@rGO was due to highly negatively charged AgNPs@rGO (−19.0 mV) composites (Table S2†). However, in case of the AuNPs on rGO sheets, the variability in shape (spherical, triangular and hexagonal) resulted in higher dissociation constants compared to PtNPs@rGO and PdNPs@rGO composites. The higher affinity of ErbB2 for immobilized antibody is an important factor in enhancing sensitivity and long-term stability of a biosensing device. Compared to chemically derived composites, the higher K_a and n for all green derivative composites suggested higher affinity and the multilayer adsorption of anti-ErbB2 can be related to the green-corona formed in presence of phytochemicals coating on G-mNPs@rGO. The proteins phytochemicals absorbed on the surface of mNPs@rGO perhaps acted as "tentacles" assisting in the attachment of additional biomolecules. The excellent association constants (K_a) of green derivative mNPs-rGO as compared to chemically synthesized mNPs-rGO composites indicated stable conjugation of protein molecules, and greater stability in biological environments. The bioinspired G-mNPs@rGO based biosensors thus exhibited good stability, selectivity and reproducibility for detection of cancer biomarker (see ESI for more details†).

4. Conclusions

We have demonstrated a simple, environmentally friendly, and universal route for bioinspired synthesis of 'green-corona' assisted G-mNPs@rGO composites by green reduction for quantification of breast cancer biomarker (ErbB2). The phytochemicals present in BPE have acted both as a reducing, surface modifying and stabilizing agents of mNPs on the G-rGO nanosheets. The cytotoxicity tests have shown that formation of the 'green-corona' on the bioinspired derived G-mNPs@rGO resulted in improved properties of nanomaterials, providing a favorable surface for attachment of antibodies. The excellent electrochemical properties of these bioinspired green G-mNPs@rGO composites have been used for development of a point-of-care device for breast cancer biomarker detection. The antibody conjugated mNPs-rGO composites have been found to be selective for human recombinant ErbB2 revealing a detection range of 1.0 fM to 0.5 μM of ErbB2. These biosensors are sensitive to femto-molar concentration and allow about three orders of magnitude wider range than the ELISA standard test for detection of breast cancer biomarker. The less toxic nature and protein compatible modified surface of G-mNPs@rGO provides a suitable microenvironment for immobilization of antibody molecules with better electrical conductivity as compared to that of the C-mNPs@rGO. The stability of these biosensors has been found to be improved due to green reduction of bioinspired G-mNPs@rGO composites as compared to those prepared chemically. The reduced toxicity and high sensitivity combined with specificity of these synthesized G-mNPs@rGO composites is a promising approach for development of *in vivo* and *in vitro* biosensor applications. The green-corona on G-mNPs@rGO can be employed as an alternative for drug delivery systems, overcoming the challenge of effective adherence to the cell surface due to degradation and the conformational changes of absorbed proteins.

Acknowledgements

The authors thank Director CSIR-National Physical Laboratory New Delhi, India for the facilities. The financial support received from DST, India (Grant No. DST/TSG/ME/2008/18) is gratefully acknowledged. L. D. and Md. A. A. were partially supported by the Plant Sciences Institute (PSI) at Iowa State University, Ames, Iowa, USA, through the PSI Faculty Scholar Program. S. S. acknowledges DST, India for providing INSPIRE faculty grant (Grant No. IFA14-MS-34).

References

1 K. S. Novoselov, V. Fal, L. Colombo, P. Gellert, M. Schwab and K. Kim, *Nature*, 2012, **490**, 192.
2 A. K. Geim, *Science*, 2009, **324**, 1530.
3 C. Chung, Y.-K. Kim, D. Shin, S.-R. Ryoo, B. H. Hong and D.-H. Min, *Acc. Chem. Res.*, 2013, **46**, 2211.
4 X. Li, Y. Wang, L. Shi, H. Ma, Y. Zhang, B. Du, D. Wu and Q. Wei, *Biosens. Bioelectron.*, 2017, **96**, 113.
5 X. Ren, T. Zhang, D. Wu, T. Yan, X. Pang, B. Du, W. Lou and Q. Wei, *Biosens. Bioelectron.*, 2017, **96**, 239.
6 D. Wu, Y. Liu, Y. Wang, L. Hu, H. Ma, G. Wang and Q. Wei, *Sci. Rep.*, 2016, **6**, 20511.
7 X. Li, S. Yu, T. Yan, Y. Zhang, B. Du, D. Wu and Q. Wei, *Biosens. Bioelectron.*, 2016, **89**, 1020.
8 D. Bitounis, H. Ali-Boucetta, B. H. Hong, D.-H. Min and K. Kostarelos, *Adv. Mater.*, 2013, **25**, 2258.
9 G. Eda, G. Fanchini and M. Chhowalla, *Nat. Nanotechnol.*, 2008, **3**, 270.
10 D. A. Dikin, S. Stankovich, E. J. Zimney, R. D. Piner, G. H. Dommett, G. Evmenenko, S. T. Nguyen and R. S. Ruoff, *Nature*, 2007, **448**, 457.
11 S. Pei and H.-M. Cheng, *Carbon*, 2012, **50**, 3210.
12 W. Wan, Z. Zhao, H. Hu, Y. Gogotsi and J. Qiu, *Mater. Res. Bull.*, 2013, **48**, 4797.
13 H. J. Shin, K. K. Kim, A. Benayad, S. M. Yoon, H. K. Park, I. S. Jung, M. H. Jin, H. K. Jeong, J. M. Kim and J. Y. Choi, *Adv. Funct. Mater.*, 2009, **19**, 1987.
14 X. Gao, J. Jang and S. Nagase, *J. Phys. Chem. C*, 2009, **114**, 832.
15 K.-H. Liao, Y.-S. Lin, C. W. Macosko and C. L. Haynes, *ACS Appl. Mater. Interfaces*, 2011, **3**, 2607.

16 S. Das, S. Singh, V. Singh, D. Joung, J. M. Dowding, D. Reid, J. Anderson, L. Zhai, S. I. Khondaker and W. T. Self, *Part. Part. Syst. Charact.*, 2013, **30**, 148.
17 W. Zhang, C. Wang, Z. Li, Z. Lu, Y. Li, J.-J. Yin, Y.-T. Zhou, X. Gao, Y. Fang and G. Nie, *Adv. Mater.*, 2012, **24**, 5391.
18 M. J. Fernández-Merino, L. Guardia, J. I. Paredes, S. Villar-Rodil, P. Solís-Fernández, A. Martínez-Alonso and J. M. D. Tascón, *J. Phys. Chem. C*, 2010, **114**, 6426.
19 Y. Chang, S.-T. Yang, J.-H. Liu, E. Dong, Y. Wang, A. Cao, Y. Liu and H. Wang, *Toxicol. Lett.*, 2011, **200**, 201.
20 E. L. K. Chng, Z. Sofer and M. Pumera, *Chem.–Eur. J.*, 2014, **20**, 6366.
21 A. B. Seabra, A. J. Paula, R. de Lima, O. L. Alves and N. Duran, *Chem. Res. Toxicol.*, 2014, **27**, 159.
22 S. Gurunathan, J. W. Han, J. H. Park, V. Eppakayala and J. H. Kim, *Int. J. Nanomed.*, 2014, **9**, 363.
23 S. Thakur and N. Karak, *Carbon*, 2015, **94**, 224.
24 S. Iravani, *Green Chem.*, 2011, **13**, 2638.
25 Z. Bo, X. Shuai, S. Mao, H. Yang, J. Qian, J. Chen, J. Yan and K. Cen, *Sci. Rep.*, 2014, **4**, 4684.
26 S. Thakur and N. Karak, *Carbon*, 2012, **50**, 5331.
27 Q. Mu, G. Su, L. Li, B. O. Gilbertson, L. H. Yu, Q. Zhang, Y.-P. Sun and B. Yan, *ACS Appl. Mater. Interfaces*, 2012, **4**, 2259–2266.
28 R. Augustine, N. Kalarikkal and S. Thomas, *Appl. Nanosci.*, 2014, **4**, 809.
29 K. Srinivasan, *Crit. Rev. Food Sci. Nutr.*, 2007, **47**, 735.
30 R. S. Vijayakumar, D. Surya and N. Nalini, *Redox Rep.*, 2004, **9**, 105.
31 R. Mittal and R. L. Gupta, *Methods Find. Exp. Clin. Pharmacol.*, 2000, **22**, 271.
32 J. Singh, R. K. Reen and F. J. Wiebel, *Cancer Lett.*, 1994, **86**, 195.
33 R. Zan, U. Bangert, Q. Ramasse and K. S. Novoselov, *Small*, 2011, **7**, 2868.
34 C. Xu, X. Wang and J. Zhu, *J. Phys. Chem. B*, 2008, **112**, 19841.
35 R. Kou, Y. Shao, D. Mei, Z. Nie, D. Wang, C. Wang, V. V. Viswanathan, S. Park, I. A. Aksay and Y. Lin, *J. Am. Chem. Soc.*, 2011, **133**, 2541.
36 P. V. Kamat, *J. Phys. Chem. Lett.*, 2009, **1**, 520.
37 S. Guo, D. Wen, Y. Zhai, S. Dong and E. Wang, *ACS Nano*, 2010, **4**, 3959.
38 M. A. Ali, K. Kamil Reza, S. Srivastava, V. V. Agrawal, R. John and B. D. Malhotra, *Langmuir*, 2014, **30**, 4192.
39 S. Srivastava, S. Abraham, C. Singh, M. A. Ali, A. Srivastava, G. Sumana and B. D. Malhotra, *RSC Adv.*, 2015, **5**, 5406.
40 S. Dutta, C. Ray, S. Sarkar, M. Pradhan, Y. Negishi and T. Pal, *ACS Appl. Mater. Interfaces*, 2015, **5**, 8724.
41 Y. Li, W. Gao, L. Ci, C. Wang and P. M. Ajayan, *Carbon*, 2010, **48**, 1124.
42 A. Krittayavathananon, P. Srimuk, S. Luanwuthi and M. Sawangphruk, *Anal. Chem.*, 2014, **86**, 12272.
43 D. W. Boukhvalov, *Phys. Status Solidi B*, 2011, **248**, 1347.
44 K. T. Chan, J. Neaton and M. L. Cohen, *Phys. Rev. B: Condens. Matter Mater. Phys.*, 2008, **77**, 235430.
45 K. Nakada and A. Ishii, *Graphene Simulation*, ed. Jian Ru Gong, 2011, p. 978.
46 V. C. Sanchez, A. Jachak, R. H. Hurt and A. B. Kane, *Chem. Res. Toxicol.*, 2012, **25**, 15.
47 J. M. Mates, *Toxicology*, 2000, **153**, 83.
48 Q. Zhang, E. Park, K. Kani and R. Landgraf, *Proc. Natl. Acad. Sci. U. S. A.*, 2012, **109**, 13237.
49 N. A. Mansor, Z. M. Zain, H. H. Hamzah, M. S. A. Noorden, S. S. Jaapar, V. Beni and Z. H. Ibupoto, *Open J. Appl. Biosens.*, 2014, **3**, 9.
50 S. Myung, A. Solanki, C. Kim, J. Park, K. S. Kim and K. B. Lee, *Adv. Mater.*, 2011, **23**, 2221.
51 C. Baj-Rossi, G. D. Micheli and S. Carrara, *Sensors*, 2012, **12**, 6520.
52 R. Guntupalli, R. S. Lakshmanan, M. L. Johnson, J. Hu, T.-S. Huang, J. M. Barbaree, V. J. Vodyanoy and B. A. Chin, *Sensing and Instrumentation for Food Quality and Safety*, 2007, **1**, 3.